

Leveraging Ligand and Composition Effects: Morphology-Tailorable Pt–Bi Bimetallic Aerogels for Enhanced (Photo-)Electrocatalysis

Geng Xue, Yueqi Li, Ran Du,* Jinying Wang,* René Hübner, Meng Gao, and Yue Hu*

Metal aerogels (MAs) are emerging porous materials displaying unprecedented potential in catalysis, sensing, plasmonic technologies, etc. However, the lack of efficient regulation of their nano-building blocks (NBBs) remains a big hurdle that hampers the in-depth investigation and performance enhancement. Here, by harmonizing composition and ligand effects, Pt- and Bi-based single- and bimetallic aerogels bearing NBBs of controlled dimensions and shapes are obtained by facily tuning the metal precursors and the applied ligands. Particularly, by further modulating the electronic and optic properties of the aerogels via adjusting the content of the catalytically active Pt component and the semiconducting Bi component, both the electrocatalytic and photoelectrocatalytic performance of the Pt–Bi aerogels can be manipulated. In this light, an impressive catalytic performance for electro-oxidation of methanol is acquired, marking a mass activity of 6.4-fold higher under UV irradiation than that for commercial Pt/C. This study not only sheds light on in situ manipulating NBBs of MAs, but also puts forward guidelines for crafting high-performance MAs-based electrocatalysts and photoelectrocatalysts toward energy-related electrochemical processes.

1. Introduction

Metal aerogels (MAs), emerging as one of the youngest members in the aerogel family, embrace the porous and self-supported structure of aerogels as well as the outstanding electrical conductivity, catalytic activity, and unique optical properties of metals.^[1–3] Hence, they manifest vast potential in applications such as electrocatalysis,^[4,5] sensing,^[6,7] and surface-enhanced Raman scattering.^[8,9] While excellent electrocatalytic properties have been widely documented, manipulating optical features of MAs for extended applications (e.g., photoelectrocatalysis) is rarely probed and the performance enhancement with light is quite limited.^[10,11] To address it, the critical challenge lies in on-target tailoring the microstructures and physical properties of the MAs, as well as the in-depth investigation of the principles for the performance optimization.

Generally, MAs are prepared from aqueous solutions of metal salts or metallic nano-building blocks (NBBs) through the sol–gel method. The majority of reported MAs, such as Au, Ag, Pd, Pt, Rh, Ni₉₇Bi, Au–Bi, Pd–Bi, and Bi–Sn, showcase nanowires (NWs)-fused network structures.^[3,5,12–15] The diameter of the NWs, also denoted as the ligament size or feature size, has been successfully tuned by applying specific initiators, altering the nanoparticles (NPs)-ions interactions, and manipulating the ligand chemistry.^[16–19] However, bearing only NWs as NBBs can largely restrict the comprehensive investigation of the structure–property correlations and the performance optimization. To address the above issues, several approaches have been proposed. In one way, special metal NPs (e.g., Ag nanoshells and Pd–Ni hollow nanospheres) were pre-synthesized as shape-tailored NBBs, followed by assembling to metal gels with two-level structures.^[20,21] Another method creates special microstructures by post-treating the as-prepared MAs.^[22–24] For example, Liu et al. demonstrated that applying H₂PtCl₆ to an Ag aerogel can yield a nanotubular-structured Pt–Ag aerogel.^[23] To avoid the time-consuming procedures involved in the aforementioned methods, in situ structure regulation has also been investigated sporadically. For instance, following an “adsorption-decomposition” growth mode, Pd aerogels structured from 2D NBBs were fabricated by using CO as both reductant and

G. Xue, M. Gao, Y. Hu
Key Laboratory of Carbon Materials of Zhejiang Province
College of Chemistry and Materials Engineering
Wenzhou University
Wenzhou 325000, P. R. China
E-mail: yuehu@wzu.edu.cn

Y. Li, R. Du
School of Materials Science and Engineering
Key Laboratory of High Energy Density Materials of the Ministry of Education
Beijing Institute of Technology
Beijing 100081, P. R. China
E-mail: rdu@bit.edu.cn

J. Wang
Network for Computational Nanotechnology
Purdue University
West Lafayette, IN 47907, USA
E-mail: wang4205@purdue.edu

R. Hübner
Helmholtz-Zentrum Dresden-Rossendorf
Institute of Ion Beam Physics and Materials Research
Bautzner Landstrasse 400, 01328 Dresden, Germany

 The ORCID identification number(s) for the author(s) of this article can be found under <https://doi.org/10.1002/sml.202301288>

DOI: 10.1002/sml.202301288

coordination reagent.^[25] Recently, our group successfully prepared several core–shell-structured bimetallic aerogels by controlling the nucleation step through manipulating the feeding order of the reactants.^[16,26] However, the as-used CO is toxic and the available NBBs are very limited. Hence, it is urgent to develop efficient and facile strategies for crafting MAs with novel and tailorable NBBs, so as to facilitate the investigation of structure–performance correlations.

In the field of nanocrystals, the ligand chemistry has been extensively investigated for modulating dimensions, shapes, and facets of the nanomaterials.^[27] However, passivation effects of the ligands can retard the fusion of NBBs and thus the development of 3D networks, which seems incompatible with MAs fabrication. Recently, limited examples successfully addressed this issue by adopting strong destabilizers to overcome the passivation effects of ligands, which yielded small-sized MAs (e.g., ≈ 3.5 nm for Au aerogels^[19]). However, the highly affinitive ligands are difficult to remove and the dimensions of NBBs remain unchanged.

In this study, sodium citrate—a commonly used moderate, low-cost, and environment-friendly ligand—was applied. Impressively, in conjunction with composition modulation, a distinct ligand effect on the dimension and shapes of NBBs was found and MAs with 0D, 1D, 2D, and 3D NBBs were obtained accordingly. Particularly, by further adjusting the electronic/optic properties via tuning the proportion of the catalytically active Pt and the semiconducting Bi component, both the electrocatalytic and photoelectrocatalytic performance of the Pt–Bi aerogels can be facilely manipulated. Using the methanol oxidation reaction (MOR) as a model reaction, the optimized Pt₁Bi₂ aerogel delivered a 6.4-fold higher current density under UV irradiation than commercial Pt/C, outperforming all reported MAs to date. This study not only provides new routes for in situ tailoring dimensions and shapes of NBBs, but also puts forward clear design guidelines for boosting the catalytic performance of MAs toward energy-related electrochemical processes.

2. Results and Discussion

2.1. Synthesis and Characterization of Aerogels

Previously, certain studies reported the synthesis of Bi-containing single-metallic and bimetallic (e.g., Cu–Bi, Ni–Bi, Sn–Bi, and Pd–Bi) aerogels.^[5,12,14,28] As summarized in Table S1, a relatively high concentration of metal sources ($c_M > 2$ mM) was usually required. The high precursor concentration may retard the acquirement of regular and small nanostructures, not to mention an efficient structure control of the NBBs.

Here, Bi, Pt, and Pt–Bi hydrogels were prepared by an excessive-NaBH₄-triggered gelation strategy proposed by our group, which features a strong destabilization capacity.^[17] In this light, a low c_M of 0.2 mM is sufficient to initiate the gelation process, facilitating effective structure control. As seen from Figure 1a and Figure S1, Supporting Information, hydrogels and the corresponding monolithic aerogels were acquired with or without the presence of sodium citrate (NaCA) as ligands. Here, the as-prepared aerogels with different formulas are denoted as Pt_xBi_y-L/M, where x and y are the proportions of Pt and Bi, respectively, and L/M indicates the molar ratio of the ligands to the

total metals. The samples without using ligands are denoted as Pt_xBi_y.

Generally, both the chemical composition and the adopted ligands can substantially affect the nanostructures of the aerogels. On the one hand, the composition effect is explored by comparing ligand-free Bi, Pt, and Pt_xBi_y aerogels. As shown in Figure 1b, Figures S2, S3, Table S2, Supporting Information, the Bi aerogel possesses 2D nanosheet-like NBBs (average lateral size of ≈ 910 nm and thickness of ≈ 16 nm), while the Pt aerogel is structured from 0D solid nanoparticles (NPs) with a diameter of (36.5 ± 3.5) nm. Intriguingly, the NBBs of the Pt_xBi_y aerogels considerably differ from those of the Bi and Pt aerogels (Figure 1c; Figure S4, Supporting Information). With 25% Pt, the Pt₁Bi₃ aerogel shows NBBs combining the morphology of nanosheets and NPs. Further increasing the Pt proportion generates a class of unique NBBs, which are composed of 3D microspheres assembled from NP-linked NWs. Though with a similar diameter of ≈ 500 nm, the microspherical unit changes from loosely compacted to closely compacted with increasing Pt proportion from 33.3% for Pt₁Bi₂ to 75.0% for Pt₃Bi₁. Such substantial composition-dependent morphological transition behavior and the yielded unique NBBs (e.g., microspheres) have never been observed for other MAs, which may point out a new dimension for crafting NBBs with desirable dimensions and novel structures. As shown in Figure S5, Supporting Information, the specific surface areas (SSAs) of the Pt_xBi_y aerogels are comparable among each other (20.6 – 21.7 m² g⁻¹), but are larger than those of the single-component Pt and Bi aerogels (< 15 m² g⁻¹) due to their highly porous microspherical NBBs.

On the other hand, the ligand effect—by adopting NaCA, a widely used ligand with a moderate binding strength—is also found to efficiently impact the structure of the NBBs. Here, the Bi, Pt, and Pt₁Bi₁ systems are picked up for demonstration. As seen from Figure 1d–f and Figures S3, S6, Supporting Information, applying 10-equivalent NaCA has no evident effect on the Pt aerogels, while it can considerably affect the NBBs of the Bi and Pt₁Bi₁ aerogels. By increasing L/M from 0 to 10, the NBBs transfer from 2D nanosheets to irregular matter for the Bi system, while from 3D microspheres to 1D NWs for the Pt₁Bi₁ system. Ex situ TEM experiments further elucidate the evolution process for the Pt₁Bi₁ and Pt₁Bi₁-10/1 aerogels (Figure S7, Supporting Information). For Pt₁Bi₁, large 2D sheet-like structures initially form upon reaction, which then gradually grow up to 3D microspheres composed by 2D sheets. As for Pt₁Bi₁-10/1, the nanowire-fused networks continuously grow larger with prolonged time. Other Pt_xBi_y systems manifest a similar phenomenon (Figures S8, S9, Supporting Information), and the ligament size for ligand-involved systems is positively correlated to the proportion of Bi (≈ 6.3 nm for Pt₃Bi₁-10/1 to ≈ 10.0 nm for Pt₁Bi₃-10/1). As revealed by nitrogen adsorption tests, the ligament size of ligand-mediated-prepared Pt_xBi_y aerogels is negatively correlated to the SSA, where the largest value (38.2 m² g⁻¹) is acquired for the Pt₂Bi₁-10/1 aerogel. Note that although the ligand chemistry has been adopted to adjust the ligament size of MAs,^[17,19] such distinct ligand-mediated morphological and dimensional changes on the NBBs have not been observed in MAs systems so far.

To further explore the morphology transition process, different amounts of ligands were applied. For the Bi system (Figure S10 and Table S2, Supporting Information), the lateral size of

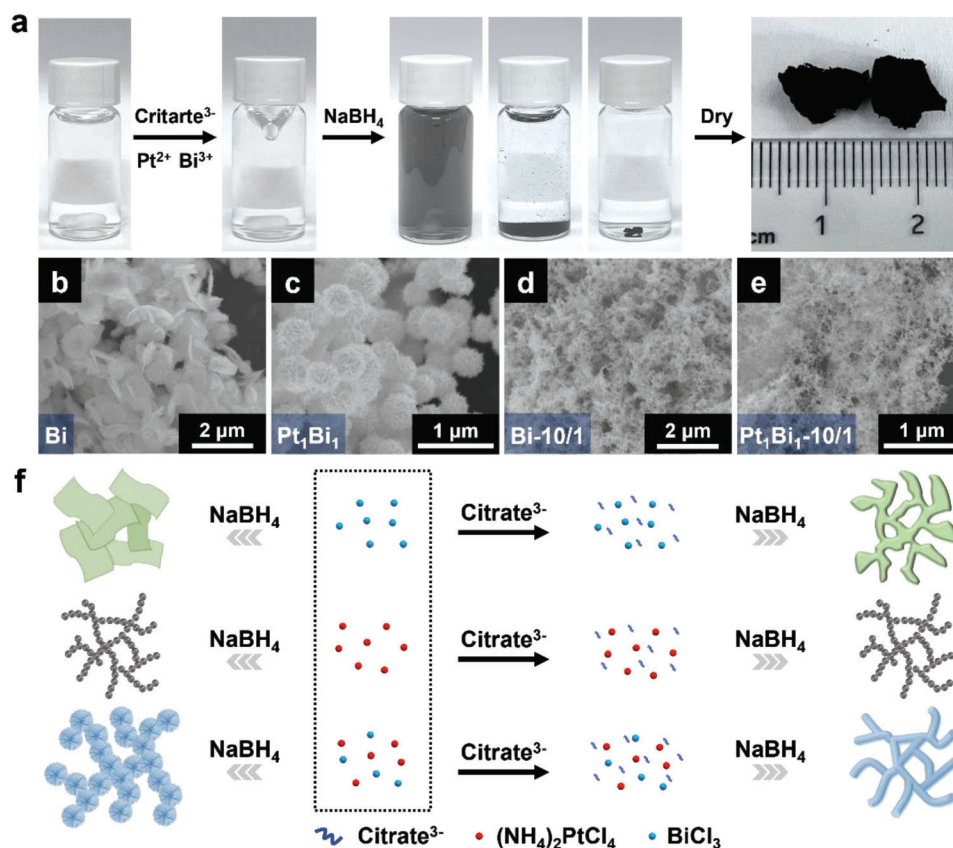


Figure 1. Fabrication of Pt–Bi aerogels with tailored NBBs. a) Photographs from the fabrication of the Pt₁Bi₁-10/1 aerogel. b–e) SEM images showing the composition-directed regulation of the NBBs of the aerogels and f) scheme of the fabrication process.

the 2D nanosheets decreases from ≈ 910 nm to ≈ 620 nm with increasing L/M from 0 to 0.01. Increasing L/M to 0.1 results in smaller irregularly shaped particles, the size of which decreases by further raising the proportion of the ligands. For the Pt₁Bi₁ system (Figure 2a–f; Figure S11, Supporting Information), however, with increasing L/M from 0 to 0.02, NWs gradually appear in company with a decreasing diameter of the microspheres (from 520 to 150 nm), unambiguously reflecting the transition from 3D microspheres to 1D NWs. Further raising L/M to 0.1 or larger leads to the formation of bare-NWs-structured networks with a ligament size of ≈ 7.3 nm. The aforementioned phenomenon can be rationalized by the selective adsorption of ligands on specific facets, which has been well documented in the literature of nanocrystals^[27] while seldomly discussed in the field of MAs.

The morphology change of the NBBs can be also evidenced from X-ray diffraction (XRD). For the Bi aerogel, as displayed in Figure 2g and Figure S12, Supporting Information, with increasing L/M from 0 to 10, a gradual intensity decrease of the Bi 104 diffraction peak (at $2\theta = 37.9^\circ$) was observed compared to other diffraction maxima (e.g., 012 and 110, $2\theta = 27.1^\circ$ and 39.6° , respectively). As for the Pt_xBi_y aerogels, most Bi is bound in Bi₂O₂CO₃ (PDF#41-1488) (Figure S13, Supporting Information), which may come from the hydrolysis of Bi followed by the reaction with atmospheric CO₂. Similarly, a change in the relative peak intensity was found. Here, the relative intensity of the 013 ($2\theta = 30.2^\circ$) and 110 ($2\theta = 32.7^\circ$) diffraction peaks is reduced by

applying 10-equivalent NaCA. However, because XRD can only give the bulk information about the crystal structure rather than the information of facets, an unambiguous understanding of the change in diffraction peaks and the corresponding shape transition cannot be identified at this stage.

Apart from the shape transition, the spatial element distribution of the aerogels was also analyzed to fully reveal the structure attribute of the aerogels. As demonstrated in Figure 3a–c, high-angle annular dark-field scanning transmission electron microscopy (HAADF-STEM) imaging and spectrum imaging analysis based on energy-dispersive X-ray spectroscopy (EDX) indicate that Pt, Bi, and O are distributed uniformly within the microspherical units. To our surprise, a distinct Bi–Pt core–shell structure was identified for the NWs (Figure 3c; Figures S14, S15, Supporting Information). This core-shell architecture is also evidenced by X-ray photoelectron spectroscopy (XPS) analysis. As shown in Figure 3d,e and Figure S16, Supporting Information, certain high-oxidation-state species (Pt (II) and Bi(III)) were detected for all aerogels due to partial oxidation during synthesis. As summarized in Table S3 and Figure S17, Supporting Information, compared to the Pt_xBi_y aerogels featuring microspheres as NBBs, more oxidized Pt and more metallic-state Bi were found in the Pt_xBi_y-10/1 aerogels. This can be explained by the fact that the exposed Pt shell is more susceptible to oxidation compared to the inner Bi core in the latter. Additionally, the detected Pt proportion of the Pt_xBi_y-10/1 aerogels is slightly larger than that of the Pt_xBi_y aerogels,

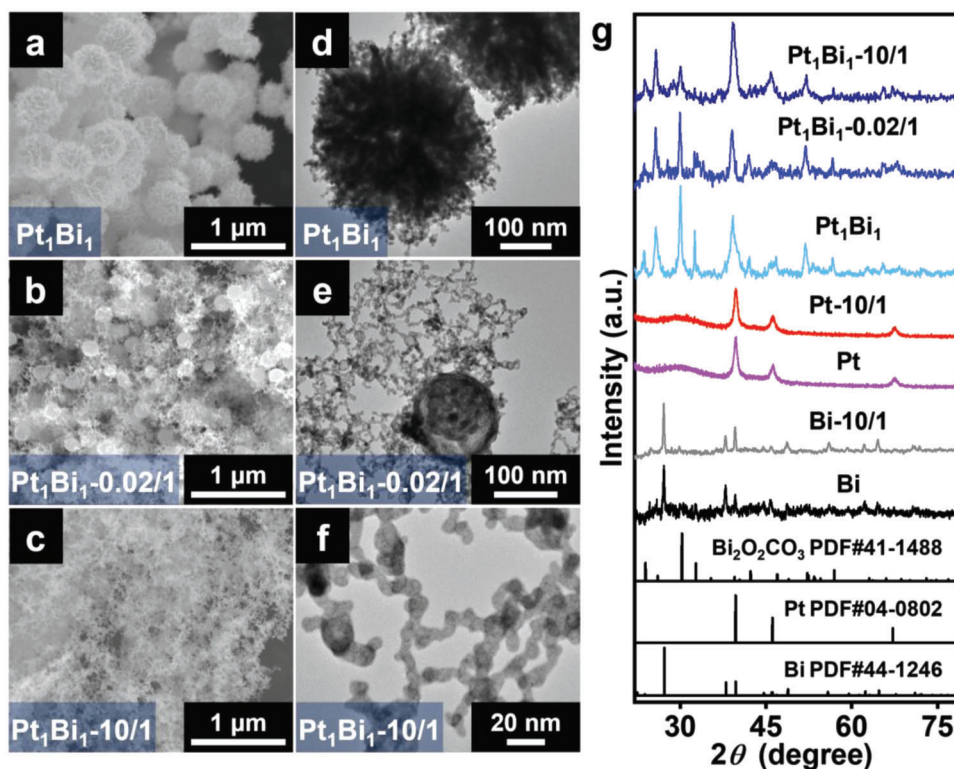


Figure 2. Ligand-directed regulation of the aerogel NBBs. a–c) SEM images, d–f) TEM images, and g) XRD patterns of the indicated aerogels.

which is ascribed to the surface-sensitive nature of the XPS technique. One potential reason for the formation of such core-shell NWs can be attributed to the kinetically preferable reduction of BiCl_3 compared to that of $(\text{NH}_4)_2\text{PtCl}_6$, though the latter features a higher reduction potential (0.199 vs 0.758 V).^[29]

2.2. Electrocatalytic and Photoelectrocatalytic Performance

MAs have been explored in diverse electrocatalytic reactions, while the utilization of their optical features to enhance the electrocatalysis performance has only been sporadically investigated. Here, a combination of catalytically active Pt and optically active Bi species may offer new insights for identifying the guideline for on-target modulating and optimizing MAs-based electrocatalysts and photoelectrocatalysts. In this study, the methanol oxidation reaction (MOR), which is the anode reaction for the direct methanol fuel cell,^[30] is used as a model reaction. For MOR, the peaks of the forward scan and the backward scan in the CV curve characterize the oxidation of the methanol and the intermediate generated during the forward scan, respectively.^[16] The peak current density of the forward scan (I_f) is often used to evaluate the catalytic activity.

At the beginning, the electrocatalytic properties for MOR are evaluated from composition and structure aspects. First, the composition effect of the aerogels is explored. As shown in Figures S18, S19, Supporting Information, I_f is positively correlated to the proportion of Pt, which increases from 1.80 $\text{A mg}_{\text{Pt}}^{-1}$ for the Pt_1Bi_2 aerogel to 3.05 $\text{A mg}_{\text{Pt}}^{-1}$ for the Pt_2Bi_1 aerogel, all of which

surpass that of commercial Pt/C (0.70 $\text{A mg}_{\text{Pt}}^{-1}$). This trend can be attributed to both the low electrical resistivity (10.6 $\mu\Omega \text{ cm}^{-1}$ for Pt vs 129 $\mu\Omega \text{ cm}^{-1}$ for Bi^[29]) and the intrinsically high electrocatalytic MOR activity of the metallic Pt. Electrochemical impedance spectroscopy (EIS) measurements suggest a negative correlation between the charge-transfer resistance (R_{ct}) and the Pt proportion of the aerogels (Figure S20, Supporting Information), further supporting the above analysis.

Second, the structure effects of the NBBs are studied by using the Pt_1Bi_1 aerogel systems, where the NBBs were adjusted by ligands as discussed in the previous sections. As shown in Figure 4a, I_f monotonously increases from 1.94 $\text{A mg}_{\text{Pt}}^{-1}$ for the Pt_1Bi_1 aerogel to 2.09 $\text{A mg}_{\text{Pt}}^{-1}$ for the $\text{Pt}_1\text{Bi}_1\text{-}0.02/1$ aerogel, and to 2.30 $\text{A mg}_{\text{Pt}}^{-1}$ for the $\text{Pt}_1\text{Bi}_1\text{-}10/1$ aerogel. This trend can be explained from two aspects. On the one hand, for the microspherical NBBs of the Pt_1Bi_1 aerogel, it is hard to form a well-connected conductive network compared to the 1D NWs-structured $\text{Pt}_1\text{Bi}_1\text{-}10/1$ aerogel. On the other hand, the Bi–Pt core-shell NWs in the $\text{Pt}_1\text{Bi}_1\text{-}10/1$ aerogel can largely expose catalytically active Pt sites, further promoting the performance. These analyses are supported by the charge-transfer resistances R_{ct} derived from the Nyquist plots. As illustrated in Figure 4b, R_{ct} decreases considerably from 162 Ω for the microspheres-constructed Pt_1Bi_1 aerogel to 96 Ω for the NWs-constructed $\text{Pt}_1\text{Bi}_1\text{-}10/1$ aerogel, suggesting enhanced electrochemical kinetics for the latter.

To further consolidate the NBBs-dependent electrocatalytic behavior, the Pt_1Bi_2 and Pt_2Bi_1 systems were tested (Figure 4c; Figure S19, Supporting Information), which follow the same trend as the Pt_1Bi_1 systems. It is worth mentioning that

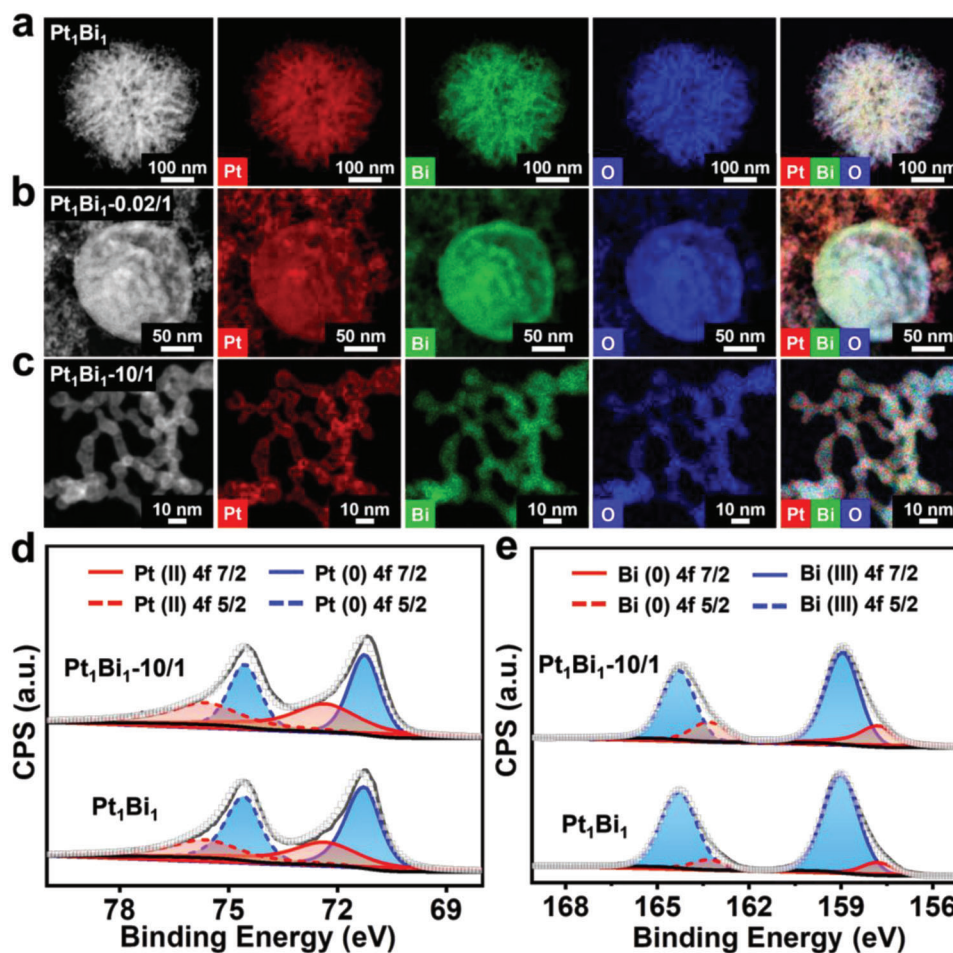


Figure 3. Element analysis of Pt–Bi aerogels. a–c) HAADF-STEM images and the corresponding STEM-EDX element distribution maps of the Pt₁Bi₁, Pt₁Bi_{1-0.02/1}, and Pt₁Bi_{1-10/1} aerogels. d,e) Deconvoluted high-resolution XPS Pt 4f and Bi 4f spectra of the indicated aerogels.

featuring both a high Pt proportion as well as Bi–Pt core-shell NWs-made NBBs, the Pt₂Bi_{1-10/1} aerogel displays the highest I_f of 3.69 A mg_{Pt}⁻¹, which is 5.3 times higher than that of commercial Pt/C (0.70 A mg_{Pt}⁻¹). This excellent activity results from the synergy of the intrinsic activity of Pt and the structure-modulation function of Bi. The proportion of intrinsically active Pt is quite high (66.7%), offering sufficient catalytically active species. Meanwhile, the proper inclusion of Bi not only promotes the formation of Bi–Pt core-shell NWs-made NBBs, but also endows the Pt₂Bi_{1-10/1} aerogel with a large SSA (38.2 m² g⁻¹), which jointly promote the exposure of catalytically active Pt sites. The chronoamperometric test further validates the superior performance of the Pt₂Bi_{1-10/1} aerogel, where a current retention of 26.9% for the Pt₂Bi_{1-10/1} aerogel and of 13.9% for commercial Pt/C were obtained after operating for 10 000 s (Figure S21, Supporting Information). The enhanced stability can be attributed to the robust network structure of the aerogel, which avoids potential detachment of the catalyst and the corrosion of the carbon substrate that is frequently encountered for commercial Pt/C.^[15]

Afterward, photoelectrocatalytic properties are studied. Here, taking the unique optical features of nano-metal-composed aero-

gels, the electrocatalytic performance was further enhanced by applying light. We have previously found that a white-light LED can promote the electrocatalytic activity of noble metal aerogels, presumably by utilizing the plasmonic effects of the nanostructured noble metals and the thermal effect stepped from the porous gel network.^[10,11] However, the enhancement was limited to less than 45%. Here, a UV light source (320–500 nm) was deliberately selected to suit the features of the Pt–Bi aerogels, substantially boosting the electrocatalytic performance. As shown in Figure 4d and Figures S22–S24, Supporting Information, all tested samples exhibit light-enhanced performance. Particularly, a remarkable I_f of 11.98 A mg_{Pt}⁻¹ was acquired for the Pt₁Bi₂ aerogel, which is 6.4-fold higher than that for Pt/C worked in the dark and under UV irradiation, respectively (Figure 4e). As summarized in Table S4, Supporting Information, this MOR performance largely surpasses not only the reported metal aerogels (e.g., 2.99 A mg_{Pd}⁻¹ for a Pd aerogel, 4.73 A mg_{Pt}⁻¹ for a Pt₁Cu₁Ir_{0.04} aerogel, and 1.83 A mg⁻¹ for a Ni_{0.7}Bi₃ aerogel),^[12,31,32] but also many noble-metal-based photoelectrocatalysts (e.g., 0.74 A mg_{Pt}⁻¹ for Pt–CdS/N–GQDs (200 mW cm⁻² Xenon lamp at $\lambda > 400$ nm) and 2.75 A mg_{Pt}⁻¹ for a Pt–Mxene–TiO₂ (50 mW cm⁻² at $\lambda = 365$ nm)).^[33,34]

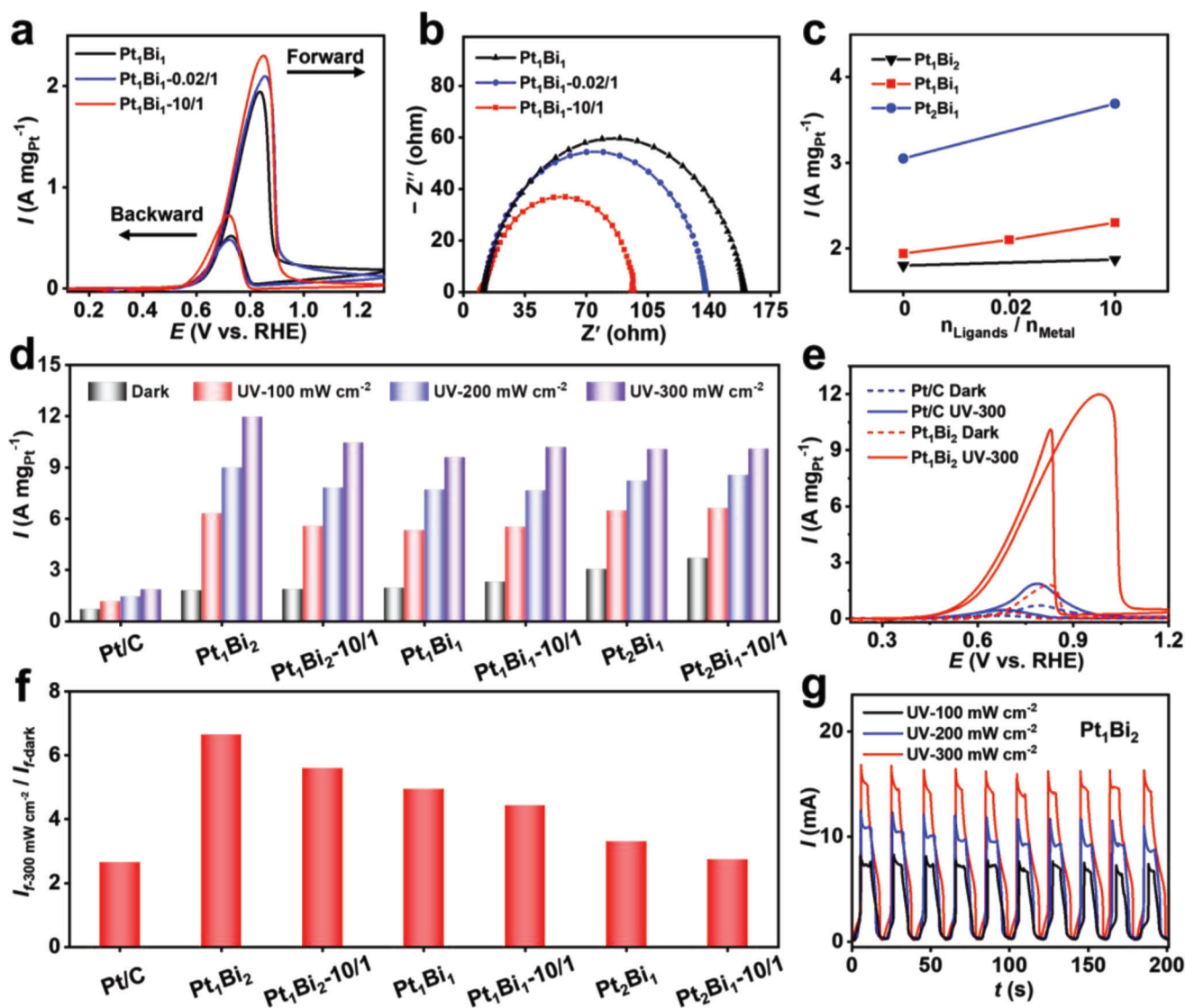


Figure 4. Electrochemical and photoelectrochemical properties of various Pt–Bi aerogels. a,b) CV curves (scan rate of 50 mV s^{-1}) and Nyquist plots of the indicated aerogels. c) Plot of I_f versus L/M for different aerogels. d) Summary of I_f for various Pt–Bi aerogels and commercial Pt/C performed under UV irradiation at various power densities. e) Comparison of the electrocatalytic and photoelectrocatalytic performance of the Pt_1Bi_2 aerogel and commercial Pt/C. f) Enhancement factors of diverse Pt–Bi aerogels and Pt/C. g) Light response behavior of the Pt_1Bi_2 aerogel electrode during a chronoamperometry test. All tests were performed in nitrogen-saturated $1.0 \text{ M KOH} + 1.0 \text{ M methanol}$ aqueous solution.

The outstanding photoelectrocatalytic performance of the Pt–Bi systems inspires us to further investigate the underlying mechanisms. Here, several effects may contribute. First, aerogels can efficiently trap light, where the light will eventually transform into heat through multiple reflections and scattering in the nanoporous network.^[16] This is also evidenced from the black color of the aerogels. Second, nanostructured noble metals and the corresponding aerogels are known to generate localized surface plasmon resonances (LSPR) upon irradiation with proper light.^[9,35] However, the LSPR absorption of Pt is not located in the UV region, hence the LSPR effect should have negligible contribution to the UV-light-enhanced MOR activity. Third, certain amounts of Bi in the aerogels are in the form of semiconducting $\text{Bi}_2\text{O}_2\text{CO}_3$ (band gap of 3.0–3.5 eV, corre-

sponding to $\approx 350\text{--}410 \text{ nm}$), which can strongly absorb UV light and thus produce electron–hole pairs.^[36] The electrically conductive Pt can promote the charge separation by efficiently exiling electrons, while the remaining highly oxidative holes on the surface^[37] can thereby promote the methanol oxidation. The potential mechanisms are shown in Figures S25–S26, Supporting Information.^[38,39]

To identify the most important factor dictating the photoelectrocatalysis, the enhancement factor (EF), which is defined as the ratio of I_f acquired under 300-mW cm^{-2} UV irradiation and in the dark, is compared in Figure 4f. EFs for all aerogels (2.7–6.6) are higher than that for Pt/C (2.6), which is ascribed to the multiple enhancement mechanisms as detailed above. The EF is correlated to both the Bi proportion and the structure of the NBBs. Ris-

ing Bi proportion leads to an EF increase from 3.3 for the Pt₂Bi₁ aerogel to 6.6 for the Pt₁Bi₂ aerogel, while the Bi–Pt core–shell NW architecture can deteriorate the EF (2.8 for the Pt₂Bi₁-10/1 aerogel and 5.6 for the Pt₁Bi₂-10/1 aerogel). Hence, a higher proportion of Bi (see Table S3, Supporting Information) and less exposure of Pt (i.e., microspherical NBBs) can promote the photoelectrocatalytic performance, implying that light-induced production of oxidative holes with Bi component dominates the light-enhanced performance enhancement. Interestingly, the trend of photoelectrocatalysis is contrary to that for electrocatalysis in the dark, which suggests that the light-induced activity enhancement plays a dominating role in catalyzing MOR. In comparison with the Pt–Bi aerogels, bare Bi aerogels exhibit negligible MOR activity due to its intrinsic electrocatalytic inertness, while a clear electrooxidation peak appears upon UV irradiation (Figure S27, Supporting Information). This observation further consolidates our hypothesis that the Bi component is inactive in the dark, while it is critical to induce photoelectric catalysis in conjunction with the Pt component under light exposure. This means the design guidelines for MA-based electrocatalysts and photoelectrocatalysts vary significantly and can be tuned by manipulating different catalytic centers.

To further utilize the light-enhanced current response, the Pt₁Bi₂ aerogel was also applied for photoelectrochemical sensing. As shown in a chronoamperometry test (Figure 4g), I_f can be switched on/off with periodic UV irradiation, demonstrating a sensitivity of $>600 \mu\text{A mW}^{-1}$ (i.e., $>8.5 \text{ A W}^{-1} \text{ cm}^{-2}$), which is more than 15-fold higher than that of previously reported Au–Pd–Pt aerogels ($40.2 \mu\text{A mW}^{-1}$).^[11] Therefore, the endeavor presented here may open up new directions in designing both high-performance MA-based photoelectrocatalysts and photoelectrochemical sensors.

3. Conclusion

To sum up, by harmonizing composition and ligand effects, monolithic Bi, Pt, and Pt–Bi aerogels structured from dimension- and shape-tailored NBBs—including 0D NPs, 1D Bi–Pt core–shell NWs, 2D nanosheets, and 3D microspheres—were crafted. By further adjusting the electronic/optic properties of the aerogels via tuning the proportion of the catalytically active Pt and the semiconducting Bi component, both electrocatalytic and photoelectrocatalytic performance were facily manipulated by using MOR as a model reaction. For electrocatalysis, the optimized Pt₂Bi₁-10/1 aerogel features a small ligament size ($\approx 5.7 \text{ nm}$) and Bi–Pt core–shell NW-based NBBs, thus enabling maximization of the catalytically active Pt sites. For photoelectrocatalysis performed under UV irradiation, however, the optimized sample is the Pt₁Bi₂ aerogel. It features microspherical NBBs and a high exposure of the light-absorbing Bi component, thus facilitating the light-induced generation of oxidative holes which can offer additional power for methanol oxidation. In this light, an outstanding I_f of up to $11.98 \text{ A mgPt}^{-1}$ was realized under 300-mW cm^{-2} UV irradiation, which is 6.4-fold higher than that for commercial Pt/C and outperforms all MAs-based MOR electrocatalysts reported to date. Moreover, the photoelectrochemical sensing property of the Pt₁Bi₂ aerogel was also evaluated, yielding an impressive sensitivity of $>8.5 \text{ A W}^{-1} \text{ cm}^{-2}$.

Therefore, the present study not only offers new routes for the in situ fabrication of NBBs-specific MAs, but also presents clear guidelines for crafting high-performance MA-based electrocatalysts and photoelectrocatalysts by maximizing specific catalytic centers. These findings should be critical for promoting fundamental and application studies of MAs and other new material systems.

Supporting Information

Supporting Information is available from the Wiley Online Library or from the author.

Acknowledgements

The use of the HZDR Ion Beam Center TEM facilities and the Analysis and Testing Center of the Beijing Institute of Technology for XRD analysis are acknowledged. This work was supported by the National Natural Science Foundation of China (22202009, 51972237), the Beijing Natural Science Foundation (2232063), the Natural Science Foundation of Zhejiang Province (LY19E020008), and the Experimental Center of Advanced Materials in Beijing Institute of Technology. Furthermore, the funding of TEM Talos by the German Federal Ministry of Education and Research (BMBF) in the framework of HEMCP (grant No. 03SF0451) is acknowledged.

Conflict of Interest

The authors declare no conflict of interest.

Data Availability Statement

The data that support the findings of this study are available from the corresponding author upon reasonable request.

Keywords

aerogels, electrocatalysis, metal aerogels, nanostructures, sol–gel process

Received: February 13, 2023

Revised: April 28, 2023

Published online:

- [1] W. Liu, A. K. Herrmann, N. C. Bigall, P. Rodriguez, D. Wen, M. Oezaslan, T. J. Schmidt, N. Gaponik, A. Eychmüller, *Acc. Chem. Res.* **2015**, *48*, 154.
- [2] X. Jiang, R. Du, R. Hübner, Y. Hu, A. Eychmüller, *Matter* **2021**, *4*, 54.
- [3] N. C. Bigall, A. K. Herrmann, M. Vogel, M. Rose, P. Simon, W. Carrillo-Cabrera, D. Dorfs, S. Kaskel, N. Gaponik, A. Eychmüller, *Angew. Chem., Int. Ed.* **2009**, *48*, 9731.
- [4] R. Du, X. Jin, R. Hübner, X. Fan, Y. Hu, A. Eychmüller, *Adv. Energy Mater.* **2019**, *10*, 1901945.
- [5] H. Wang, L. Jiao, L. Zheng, Q. Fang, Y. Qin, X. Luo, X. Wei, L. Hu, W. Gu, J. Wen, C. Zhu, *Adv. Funct. Mater.* **2021**, *31*, 2103465.
- [6] W. Gao, D. Wen, *VIEW* **2021**, *2*, 20200124.
- [7] G. Li, J. Hao, W. Li, F. Ma, T. Ma, W. Gao, Y. Yu, D. Wen, *Anal. Chem.* **2021**, *93*, 14068.
- [8] X. Gao, R. J. A. Esteves, L. Nahar, J. Nowaczyk, I. U. Arachchige, *ACS Appl. Mater. Interfaces* **2016**, *8*, 13076.

- [9] L. Zhou, Y. Peng, N. Zhang, R. Du, R. Hübner, X. Wen, D. Li, Y. Hu, A. Eychmüller, *Adv. Opt. Mater.* **2021**, 9, 2100352.
- [10] R. Du, J. O. Joswig, R. Hübner, L. Zhou, W. Wei, Y. Hu, A. Eychmüller, *Angew. Chem., Int. Ed.* **2020**, 59, 8293.
- [11] R. Du, J. O. Joswig, X. Fan, R. Hübner, D. Spittel, Y. Hu, A. Eychmüller, *Matter* **2020**, 2, 908.
- [12] A. A. Dubale, Y. Zheng, H. Wang, R. Hübner, Y. Li, J. Yang, J. Zhang, N. K. Sethi, L. He, Z. Zheng, W. Liu, *Angew. Chem., Int. Ed.* **2020**, 59, 13891.
- [13] Q. Fang, Y. Qin, H. Wang, W. Xu, H. Yan, L. Jiao, X. Wei, J. Li, X. Luo, M. Liu, L. Hu, W. Gu, C. Zhu, *Anal. Chem.* **2022**, 94, 11030.
- [14] Z. Wu, H. Wu, W. Cai, Z. Wen, B. Jia, L. Wang, W. Jin, T. Ma, *Angew. Chem., Int. Ed.* **2021**, 60, 12554.
- [15] W. Liu, P. Rodriguez, L. Borchardt, A. Foelske, J. Yuan, A. K. Herrmann, D. Geiger, Z. Zheng, S. Kaskel, N. Gaponik, R. Kotz, T. J. Schmidt, A. Eychmüller, *Angew. Chem., Int. Ed.* **2013**, 52, 9849.
- [16] R. Du, Y. Hu, R. Hübner, J. O. Joswig, X. Fan, K. Schneider, A. Eychmüller, *Sci. Adv.* **2019**, 5, eaaw4590.
- [17] R. Du, J. Wang, Y. Wang, R. Hübner, X. Fan, I. Senkovska, Y. Hu, S. Kaskel, A. Eychmüller, *Nat. Commun.* **2020**, 11, 1590.
- [18] D. Wen, W. Liu, D. Haubold, C. Zhu, M. Oschatz, M. Holzschuh, A. Wolf, F. Simon, S. Kaskel, A. Eychmüller, *ACS Nano* **2016**, 10, 2559.
- [19] J. Xu, F. Sun, Q. Li, H. Yuan, F. Ma, D. Wen, L. Shang, *Small* **2022**, 18, 2200525.
- [20] X. Gao, R. J. A. Esteves, T. T. Luong, R. Jaini, I. U. Arachchige, *J. Am. Chem. Soc.* **2014**, 136, 7993.
- [21] B. Cai, D. Wen, W. Liu, A. K. Herrmann, A. Benad, A. Eychmüller, *Angew. Chem., Int. Ed.* **2015**, 54, 13101.
- [22] B. Cai, R. Hübner, K. Sasaki, Y. Zhang, D. Su, C. Ziegler, M. B. Vukmirovic, B. Rellinghaus, R. R. Adzic, A. Eychmüller, *Angew. Chem., Int. Ed.* **2018**, 57, 2963.
- [23] W. Liu, D. Haubold, B. Rutkowski, M. Oschatz, R. Hübner, M. Werheid, C. Ziegler, L. Sonntag, S. Liu, Z. Zheng, A.-K. Herrmann, D. Geiger, B. Terlan, T. Gemming, L. Borchardt, S. Kaskel, A. Czyska-Filemonowicz, A. Eychmüller, *Chem. Mater.* **2016**, 28, 6477.
- [24] Q. Shi, C. Zhu, M. Tian, D. Su, M. Fu, M. H. Engelhard, I. Chowdhury, S. Feng, D. Du, Y. Lin, *Nano Energy* **2018**, 53, 206.
- [25] M. Z. Yazdan-Abad, M. Noroozifar, A. S. Douk, A. R. Modarresi-Alam, H. Saravani, *Appl. Catal., B* **2019**, 250, 242.
- [26] R. Du, W. Jin, H. Wu, R. Hübner, L. Zhou, G. Xue, Y. Hu, A. Eychmüller, *J. Mater. Chem. A* **2021**, 9, 17189.
- [27] A. Heuer-Jungemann, N. Feliu, I. Bakaimi, M. Hamaly, A. Alkilany, I. Chakraborty, A. Masood, M. F. Casula, A. Kostopoulou, E. Oh, K. Susumu, M. H. Stewart, I. L. Medintz, E. Stratakis, W. J. Parak, A. G. Kanaras, *Chem. Rev.* **2019**, 119, 4819.
- [28] Y. Wang, L. Cheng, Y. Zhu, J. Liu, C. Xiao, R. Chen, L. Zhang, Y. Li, C. Li, *Appl. Catal., B* **2022**, 317, 121650.
- [29] J. G. Speight, *Lange's Handbook of Chemistry* (16th ed.), McGraw-Hill, New York **2005**.
- [30] N. Yang, D. Chen, P. Cui, T. Lu, H. Liu, C. Hu, L. Xu, J. Yang, *SmartMat* **2021**, 2, 234.
- [31] C. Wang, W. Gao, X. Wan, B. Yao, W. Mu, J. Gao, Q. Fu, D. Wen, *Chem. Sci.* **2022**, 13, 13956.
- [32] Q. Fang, H. Wang, X. Lv, X. Wei, X. Luo, J. Huang, L. Jiao, W. Gu, W. Song, C. Zhu, *ACS Sustainable Chem. Eng.* **2021**, 9, 13039.
- [33] Z. He, C. Yuan, H. Gao, Z. Mou, S. Qian, C. Zhai, C. Lu, *ACS Sustainable Chem. Eng.* **2020**, 8, 12331.
- [34] Y. Sun, Y. Zhou, Y. Liu, Q. Wu, M. Zhu, H. Huang, Y. Liu, M. Shao, Z. Kang, *Nano Res.* **2020**, 13, 2683.
- [35] J. Kneipp, H. Kneipp, K. Kneipp, *Chem. Soc. Rev.* **2008**, 37, 1052.
- [36] Y. Sun, Z. Zhao, W. Zhang, C. Gao, Y. Zhang, F. Dong, *J. Colloid Interface Sci.* **2017**, 485, 1.
- [37] L. Huang, J. Zou, J. Y. Ye, Z. Y. Zhou, Z. Lin, X. Kang, P. K. Jain, S. Chen, *Angew. Chem., Int. Ed.* **2019**, 58, 8794.
- [38] J. Hu, C. Zhai, M. Zhu, *Chin. Chem. Lett.* **2021**, 32, 1348.
- [39] Z. Zhang, J. Liu, J. Wang, Q. Wang, Y. Wang, K. Wang, Z. Wang, M. Gu, Z. Tang, J. Lim, T. Zhao, F. Ciucci, *Nat. Commun.* **2021**, 12, 5235.
- [40] N. Wang, Y. Li, Q. Cui, X. Sun, Y. Hu, Y. Luo, R. Du, *Acta Phys.-Chim. Sin.* **2023**, 2212014, <https://doi.org/10.3866/pku.whxb202212014>.